Journal of Sol-Gel Science and Technology
https://doi.org/10.1007/s10971-024-06422-9

ORIGINAL PAPER

MRI-based sensing of pH-responsive content release from mesoporous silica nanoparticles

Mirjana Mundžić[1] · Jelena Lazović[2] · Minja Mladenović[1] · Aleksandra Pavlović[1] · Amelia Ultimo[3] · Oliviero L. Gobbo[3,4] · Eduardo Ruiz-Hernandez[3,4] · Maria Jose Santos-Martinez[3,4,5] · Nikola Ž. Knežević[1]

Received: 23 February 2024 / Accepted: 13 May 2024

Abstract

A proof of principle study toward developing a novel methodology which could be applicable for a non-invasive monitoring of the release of cargo molecules from therapeutic and diagnostic nanoparticles, as well as for possible monitoring of tissue pH variations. This was achieved by quantifying changes in longitudinal relaxation time (T_1) before and after the pH-responsive release of contrast agents, for magnetic resonance imaging (MRI), from the pores of mesoporous silica nanoparticles (MSNs). The pores were filled with the FDA-approved contrast agent Gadobutrol (GdB), and its retention inside the pores ensured by covalent attachment of β-cyclodextrin monoaldehyde to hydrazine-functionalized MSN, through acidification-cleavable hydrazone linkage. The release kinetics of GdB was measured by fluorescence spectroscopy which revealed that the release of the contrast agent was enhanced at pH 5.0 in comparison to the release at pH 6.0 and 7.4. Furthermore, the changes in T_1, occurring in response to the enhanced release of GdB from the pores of MSN at weakly acidic conditions, were successfully demonstrated by MRI measurements. It is envisioned that this approach using contrast agent-loaded nanoparticles before the treatment with the drug-filled analogs, could be applied in the future for tracking the locations and efficacies of nanomedicines for therapeutic cargo delivery.

Graphical Abstract

Pores of of β-maleimidopropionic acid hydrazide (BMPH)-functionalized mercaptopropyl-functionalized mesoporous silica nanoparticles (MPMSNs) were loaded with the contrast agent Gadobutrol and capped with β-cyclodextrin monoaldehyde. In weakly acidic environment the release of contrast agents was induced, and the enhanced release of GdB at pH 5.0 vs. pH 7.4 was evidenced by magnetic resonance imaging measurements.

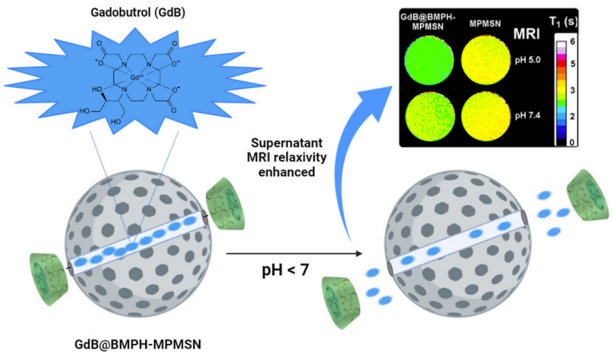

✉ Nikola Ž. Knežević
nknezevic@biosense.rs

[1] BioSense Institute, University of Novi Sad, Dr Zorana Djindjica 1, 21000 Novi Sad, Serbia

[2] Max Planck Institute for Intelligent Systems, Heisenbergstrasse 3, 70569 Stuttgart, Germany

[3] School of Pharmacy and Pharmaceutical Sciences, Panoz Institute, Trinity College Dublin, D02PN40 Dublin, Ireland

[4] Trinity St. James's Cancer Institute, St James's Hospital, D08 NHY1 Dublin, Ireland

[5] School of Medicine, Trinity College Dublin, D02 E8C0 Dublin, Ireland

Published online: 04 June 2024

Keywords MRI tracking of cargo delivery · pH-responsive delivery · Gadobutrol · MRI pH sensing · MSNs

Highlights

- Proof of concept: MRI monitors cargo release from nanoparticles as pH changes.
- Potential for real-time MRI monitoring of the delivery of nanoparticle payload.
- GdB release from MSN pores enhanced at pH 5 vs. 6 and 7.4, confirmed by fluorescence spectroscopy.

1 Introduction

Stimuli-responsive drug delivery systems (DDSs) show a great potential for the safely delivering drugs to specific target areas while avoiding the adverse effects of cytotoxic drugs [1, 2]. The application of nanotechnology in medicine also offers new opportunities for developing optimized diagnostic tools. An increasing number of novel nanoparticulate delivery systems are being developed that contain different combinations of therapeutic and diagnostic agents on the same nanoparticle (NP), allowing real-time tracking of the therapy progress [3, 4]. Hence, selective imaging of cancer tissue can be achieved by using nanoparticles containing agents such as radioluminescent materials [5], cyanine-based fluorescent dyes [6], near infra-red (NIR) fluorophores [7], radionuclides [8], or magnetic resonance imaging contrast agents (MRI-CA) [9, 10]. The major advantages of MRI over other imaging modalities include non-invasiveness, no use of ionizing radiation, extremely clear and detailed images of soft structures, deep tissue imaging and relatively rapid scanning. On the other hand, tumors typically develop low extracellular pH, which helps tumor progression, metastasis, resistance to therapy and impairs the patient's immunological response [11, 12]. Hence, there is a strong motivation for monitoring the tissue pH for the purpose of cancer diagnostics, in addition to utilizing the weakly acidic environment for triggering the drug release. Furthermore, internalization of nanoparticles typically occurs through acidification in endo/lysosomal compartments where pH may be as low as 4.5 [13].

Novel nanomaterials, such as dendritic DNA scaffolds functionalized with pH-responsive CAs have been reported for MRI-based sensing of pH [14], while a pH-activatable T_1–T_2 dual-modal MRI contrast agent, SPIO@SiO_2@MnO_2, is proposed for detection of acidic tissue environment [15]. In a recent study, the release of the MRI contrast agent gadopentetate dimeglumine from MSN mesopores was demonstrated upon exposure to high-intensity focused ultrasound, which was monitored by MRI [16]. In this work, we describe a novel MRI-based methodology concept for real-time monitoring of cargo release from pH-responsive nanocarriers. Mesoporous silica nanoparticles (MSNs) are suitable scaffolds for the construction of such nanocarriers [17], due to their facile surface functionalization, high surface area, high porosity, and particle diameter in a suitable range to potentially enhance the treatment effectiveness through the enhanced permeability and retention (EPR) effect in cancerous tissues [18]. In addition, the drug-carrying MSNs are being readily designed to release the therapeutic cargo molecules upon exposure to specific stimuli, such as intratumoral molecules, pH changes or external stimuli (e.g., light or a magnetic field) [19]. Under these circumstances, a minor release of the capped molecules is typically noted prior to exposure to the stimuli but larger amounts are released subsequently. Furthermore, the biocompatibility of MSN-based nanomedicines has been demonstrated by in vivo studies along with their capabilities to accumulate in tumors and effectively deliver anticancer drugs [20, 21].

In the current research study, mercaptopropyl-MSN (MPMSN) was synthesized and further modified to obtain a hydrazine-functionalized surface (BMPH-MPMSN, Scheme 1a). The pores of BMPH-MPMSN were then loaded with the MRI-CA gadobutrol (GdB) and entrapped by pore-blocking with β-cyclodextrin (CD) moieties and the addition of adamantylamine (AA) to seal the CD cavity through host-guest interaction (Scheme 1b) [22, 23]. The as formed hydrazone linkage between CD and BMPH-MPMSN is known to undergo hydrolysis in weakly acidic conditions [24], which enables the obtained nanomaterial to function as an acidification-responsive nanocarrier for the release of pore-entrapped GdB. Even though the use of cyclodextrin hosts such as anisidine analogs were reported for achieving pH-responsive nanogating in MSNs [25], no effect on the stability of AA-β-CD complex is expected in physiological or weakly acidic conditions due to high pKa of AA (10.7). The binding constants Ka (M^{-1}) of the AA to cyclodextrins are reported in the following ascending order: α-CD(183) < γ-CD(306) « β-CD(5150) [26]. The newly developed materials were physico-chemically characterized and the pH-responsive release kinetics of GdB was monitored by fluorescence spectroscopy. Finally, the changes in MRI relaxation occurring in response to the release of GdB were measured from the buffered suspensions of GdB-loaded material at pH 5.0 and 7.4.

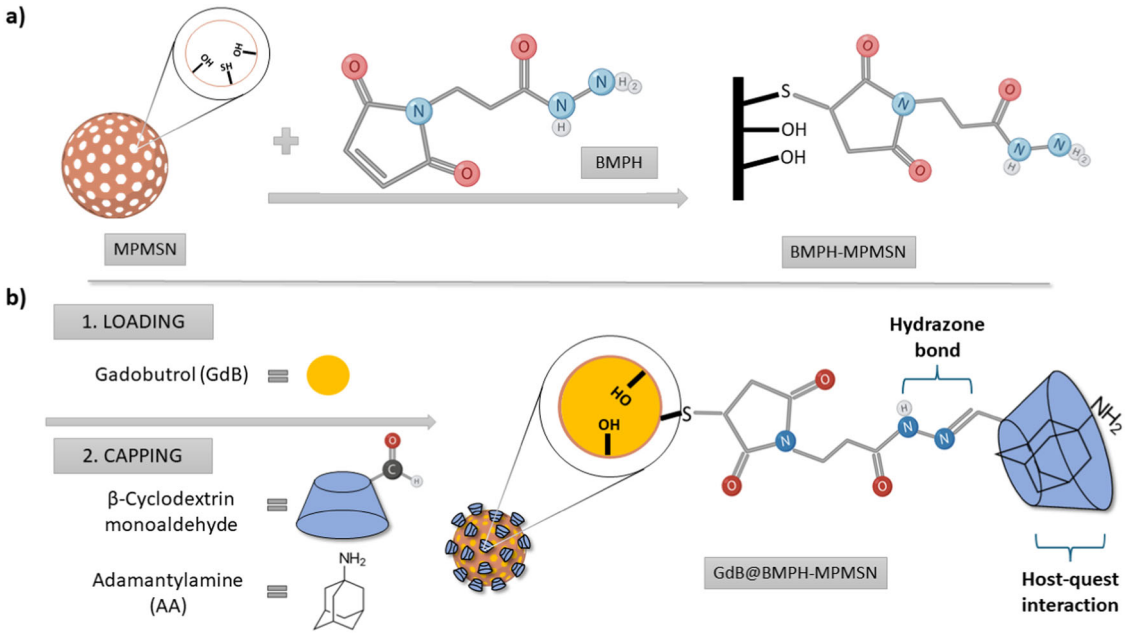

Scheme 1 **a** Formation of β-maleimidopropionic acid hydrazide (BMPH)-functionalized mercaptopropyl-MSN (MPMSN). **b** Loading of the contrast agent gadobutrol (GdB) and pore capping with β-cyclodextrin monoaldehyde (CD-CHO) and Adamantylamine (AA)

2 Materials and methods

2.1 Materials

All reagents and solvents were purchased and used as received. Tetraethoxysilane (TEOS), aminopropyl-trimethoxysilane (APTMS), mercaptopropyl trimethoxysilane (MPTMS), cetyltrimethylammonium bromide (CTAB), β-cyclodextrin (CD), Dess Martin periodinane (DMP), adamantylamine (AA), N-β-maleimidopropionic acid hydrazide (BMPH) and gadobutrol monohydrate (GdB) were purchased from Sigma-Aldrich.

2.2 Synthesis of mercaptopropyl-functionalized MSN material (MPMSN)

Cetyltrimethylammonium bromide (CTAB, 1 g, 2.74 mmol) was first dissolved in 480 mL of water. NaOH (aq) (2 M, 3.50 mL) was added to the CTAB solution, followed by adjusting the solution temperature to 80 °C. Tetraethyl orthosilicate (TEOS, 5 mL, 25.7 mmol) was first introduced dropwise to the surfactant solution, followed by dropwise addition of (3-mercaptopropyl) trimethoxysilane (MPTMS, 0.97 mL, 5.13 mmol). The mixture was allowed to stir for 2 h to give rise to a white precipitate (as-synthesized MPMSN). The solid product was filtered, washed with copious amounts of deionized water and ethanol, and dried at 80 °C to stabilize the mesoporous structure. Final mercaptopropyl-MSN material (MPMSN) was obtained upon removal of the CTAB surfactant template by extraction with a solution of concentrated HCl in methanol (1%, v/v). After 6 h of extraction, the material was additionally washed with deionized water and ethanol, and again dried at 80 °C.

2.3 Synthesis of BMPH-MPMSN

120 mg (0.4 mmol) of BMPH was dissolved in 40 mL of water followed by the addition of 800 mg of MPMSN. The mixture was stirred for 24 h at room temperature. The material was then isolated via centrifugation, washed three times with water, once with ethanol and dried at 80 °C.

2.4 Oxidation of β-cyclodextrin to CD-CHO

The procedure for oxidation of β-CD was done as previously published [27, 28]. Namely, 0.20 g of β-CD were dissolved in 5 mL of dimethyl sulfoxide (DMSO), 2 equiv. of Dess Martin periodinane (DMP) was added and the reaction mixture was stirred for 1 h at room temperature. Addition of 150 mL of acetone and cooling allowed the isolation of the crude product CD monoaldehyde by filtration.

2.5 Synthesis of GdB@BMPH-MPMSN

GdB (4 mg) was dissolved in 1 mL of PBS (10 mM, pH 7.4). BMPH-MPMSN (30 mg) was added and stirred for 24 h at room temperature in the dark. Then, 30 mg of β-CD-CHO was added, and the stirring continued for another 24 h.

Finally, 2 mg of GdB and 0.3 mmol of adamantylamine (57 mg) were stirred for 1 h in 0.5 mL of PBS and added to the MSN-containing suspension. Stirring continued for another 6 h and the mixture was then centrifuged for 10 min at 11000 rpm and washed three times with PBS. All supernatants were saved and used for the calculation of the GdB loading. The material was dried at 80 °C.

2.6 Quantification of the loaded GdB contrast agent

The amounts of loaded GdB were measured by fluorescence spectroscopy ($\lambda_{ex} = 274$ nm, $\lambda_{em} = 312$ nm), based on the prepared standard curves. The sum of the calculated amounts of GdB in the supernatants after all washings was subtracted from the initial amount of GdB which was added to the materials, to yield the loaded GdB. The formulae used to calculate the GdB concentration based on the standard curves are $I = 95.514c + 269.2$ (pH 5), $I = 143.63c + 256.95$ (pH 6) and $I = 80.292c + 590.94$ (pH 7.4), where I is the intensity of the fluorescence at 312 nm, after excitation at 274 nm.

2.7 Measurements of release kinetics of GdB

GdB release measurements were performed from suspensions at different pH (in acetate buffer at pH 5.0, and in PBS at pH 6.0 and 7.4) of the prepared materials at a concentration of 0.5 mg/mL. At predetermined time points, the suspensions were centrifuged, and the supernatants were analyzed to determine the amount of GdB released by measuring the fluorescence intensity ($\lambda_{ex} = 274$ nm, $\lambda_{em} = 312$ nm). After the measurements, the solid residues of the materials were re-dispersed in the supernatants and returned to stirring until the next time point. All measurements were performed in triplicate.

2.8 Scanning electron microscopy

SEM images were obtained using a Tescan MIRA3 XMU FESEM. The samples were previously coated with a thin layer of Au using a standard sputtering technique. Three images for each material were analyzed by ImageJ software to determine the range of particle diameters.

2.9 Transmission electron microscopy

TEM characterization was conducted in a FEI Talos F200X microscope, operated at 200 keV voltage, in conventional mode. The samples were prepared following a standard procedure where the nanoparticles were first dispersed into ethanol and then a drop of the solution was placed on a carbon-coated Cu grid, which was allowed to dry in air.

2.10 X-ray diffraction measurements

The ordering of porous structure of synthesized samples were examined using X-ray diffraction (Rigaku Ultima IV, Japan). The X-ray beam was nickel filtered CuKα1 radiation ($\lambda = 0.1540$ nm, operating at 40 kV and 40 mA). XRD data were collected from 2 to 10° (2θ) at a scanning rate of 0.5°/min, with a step size of 0.02. Bragg-Brentano focusing geometry and the scintillation detector were used to provide high-intensity, high-resolution measurements and scanning from the smallest possible angle.

2.11 Nitrogen adsorption-desorption measurements

The analyses were conducted using an Anton Paar NOVAtouch LX2 instrument after degassing materials for 6 h at 105 °C in vacuum. Brunauer–Emmett–Teller (BET) specific surface area of materials was calculated from the adsorption branch, in the relative pressure range from 0.05 to 0.3 P/P°. Barrett, Joyner and Halenda (BJH) calculations of pore diameter were performed on the desorption branch of the isotherm.

2.12 Thermogravimetric analyses

The TGA and DSC analyses were performed using a DTA-TG-DSC - Netzsch STA 449 F5 Jupiter. Typically, 5 mg of materials were measured, and the analyses were performed in a nitrogen atmosphere.

2.13 Spectrophotometric measurements

UV/VIS absorbance and fluorescence spectra were recorded on a UV-VIS spectrometer - Jasco V-750 and Spectrofluorometer - Jasco FP-8550, respectively. The measurements conditions are provided above. FTIR spectra have been obtained by the transmission KBr pellet technique using a Thermo-Nicolet Nexus 670 instrument.

2.14 Dynamic light scattering and zeta potential measurements

DLS and zeta potential of the synthesized nanoparticles were recorded on a Particle size analyzer—Litesizer 500 (Anton Paar, Graz, Austria). The hydrodynamic diameter of the starting MPMSN and BMPH-MPMSN materials was obtained by conducting the measurements on suspensions of the materials in water at a final concentration of 0.1 mg/mL in quintuplicate. Zeta potential measurements were performed in 10 mM solution of NaCl in water.

2.15 Measurement of longitudinal relaxation time (T_1)

Suspensions of the materials (10 mg/mL) were prepared in PBS buffer pH 7.4 (10 mM) and acetate buffer pH 5 (10 mM). As soon as suspensions were made, solutions were transferred to 1 mL syringes and placed in a sample holder for scanning. MRI was done using a 7-Tesla preclinical scanner (Bruker, Ettlingen, Germany) with an actively shielded gradient (BGA20SHP) system, maximum 300 mT/m gradient strength, and 40 mm quadrature birdcage coil. Longitudinal relaxation time (T_1) was measured using a saturation recovery method with a variable repetition time and rapid acquisition with relaxation enhancement (RAREVTR); TR = 0.06, 0.07, 0.08, 0.09, 0.1, 0.2, 0.3, 0.4, 0.5, 0.6, 0.7, 0.8, 0.9, 1.0, 2.0, 3.0, 4.0, 5.0, 6.0 s, echo time (TE) = 6.68 ms, RARE factor = 2, 117 μm^2 in-plane resolution, 1 mm slice thickness, NEX = 1. Image processing and T_1 quantification was done offline using ImageJ (National Institutes of Health; *imagej.nih.gov/ij/*), and the MRI analysis calculator plugin written by Karl Schmidt.

To convert measured T_1 values of BMPH-MPMSN suspensions to released GdB in mg/mL, a series of GdB solutions (0.1, 0.5, 1, 1.5 and 2 mg/mL) were prepared at two different pH values (5.0 and 7.4) and the linear curve was fitted using equation: $R_1 = R_1^\circ + r_1[GdB]$, where $R_1 = 1/T_1$ is measured relaxation rate of the GdB solution, R_1^o is the relaxation rate of buffer solution without GdB, $[GdB]$ is the concentration of GdB and r_1 is the longitudinal relaxivity of GdB calculated as a slope of the linear fit.

2.16 Statistical analysis

Analysis of variance (ANOVA) with repeated measures was used to compare R_1-values, re-calculated as concentrations of released GdB at pH 5.0 vs pH 7.4 at 0.5, 1.5, 3.5, 7.5 and 11.5 h. Bonferroni post hoc test was used to correct for multiple comparison ($p < 0.05$ considered statistically significant). OriginPro 2021 (OriginLab, USA) was used for statistical analysis.

3 Results

The MSN material was synthesized by following the well-established methodology that involves surfactant-templated and base-catalyzed co-condensation of silica precursors (TEOS and MPTMS) [29]. Further functionalization with BMPH was used as a crosslinker between mercaptopropyl-functionalized MSNs and the pore blocking agent – β-CD-CHO, which yields in entrapment of the cargo molecules (GdB) in the process (Scheme 1). β-CD-CHO was prepared by oxidation of β-CD though a known procedure [27, 28], and successful oxidation was confirmed by UV/VIS and FTIR measurements (Supplementary Fig. S1). Further reaction with AA was employed to seal the 0.78 nm cavity of β-CD through strong host-guest interactions between the adamantane and the surface-attached β-cyclodextrin moieties. Figure 1 shows the SEM and TEM images of the MPMSN and BMPH-MPMSN materials. The SEM images evidence spherical morphology of the particles with a diameter in the range of 70–250 nm, while TEM images reveal the particles in the range 70–130 nm and the structured particle porosity.

The low angle XRD measurements (Fig. 2a) revealed that the MSN material exhibits 2D-hexagonal pore structure, which is not significantly influenced after functionalization with BMPH. The presence of the BMPH functional group on the MSNs is evident from the infrared spectrum of the BMPH-MPMSN material (Fig. 2b), with the band at 1701 cm^{-1} ascribed to the stretching vibrations of the carbonyl groups of BMPH. The FTIR spectrum of GdB@BMPH-MPMSN showed this vibration band more pronounced with slight shifting to 1705 cm^{-1}, due to the presence of carbonyl bands in GdB. All other bands are fairly similar in all spectra, with the wide ν(O-H) in the region 3000–3600 cm^{-1} and δ(O-H) centered at 1635 cm^{-1} ascribed to the adsorbed water and surface silanols. The bands arising from the surface functionalized groups are evident at 2924 and 2853 cm^{-1} (ν(C-H)), 1461 and 1403 cm^{-1} (ν(C-C)), 796 cm^{-1} (ν(Si-C)) and 684 cm^{-1} (ν(C-S)). Different types of stretching Si-O vibrations are noted at 966 cm^{-1} (ν(Si-OH)) and the broad band ascribed to ν(Si-O-Si) and ν(Si-O-C), with the maximum at 1077 cm^{-1} in case of MPMSN and BMPH-MPMSN. The maximums of these bands are shifted to 958 and 1047 cm^{-1}, respectively, in the case of GdB@BMPH-MPMSN. The shifting to lower energy of vibration of these bands could be ascribed to the presence of GdB on the surface and inside the mesopores, which slightly weakens the nearby Si-O bonds though hydrogen bonding with the silica surface. The TGA and DSC curves confirm the successful functionalization of BMPH (Supplementary Fig. S3). Even though the TGA curves show overlapping weight loss patterns, careful analysis confirms that in the case of BMPH-MPMSN material there is an additional 1% weight loss (Table 1, obtained by subtracting weight loss at 300 and 700 °C), in comparison to the starting MPMSN, which can be ascribed to the functionalized BMPH group. In case of GdB-loaded materials the weight loss in the same range equals 27.6%. The DSC curves clearly show a pronounced endothermic band centered around 560 °C, which further evidences the presence of BMPH. In case of the GdB-loaded material, substantial exothermic change is observed after 527 °C, which can be ascribed to the pore-capping and loaded molecules. The hydrodynamic diameter of the particles and their zeta potential, as measured in aqueous suspension at 0.1 mg/mL do not change significantly

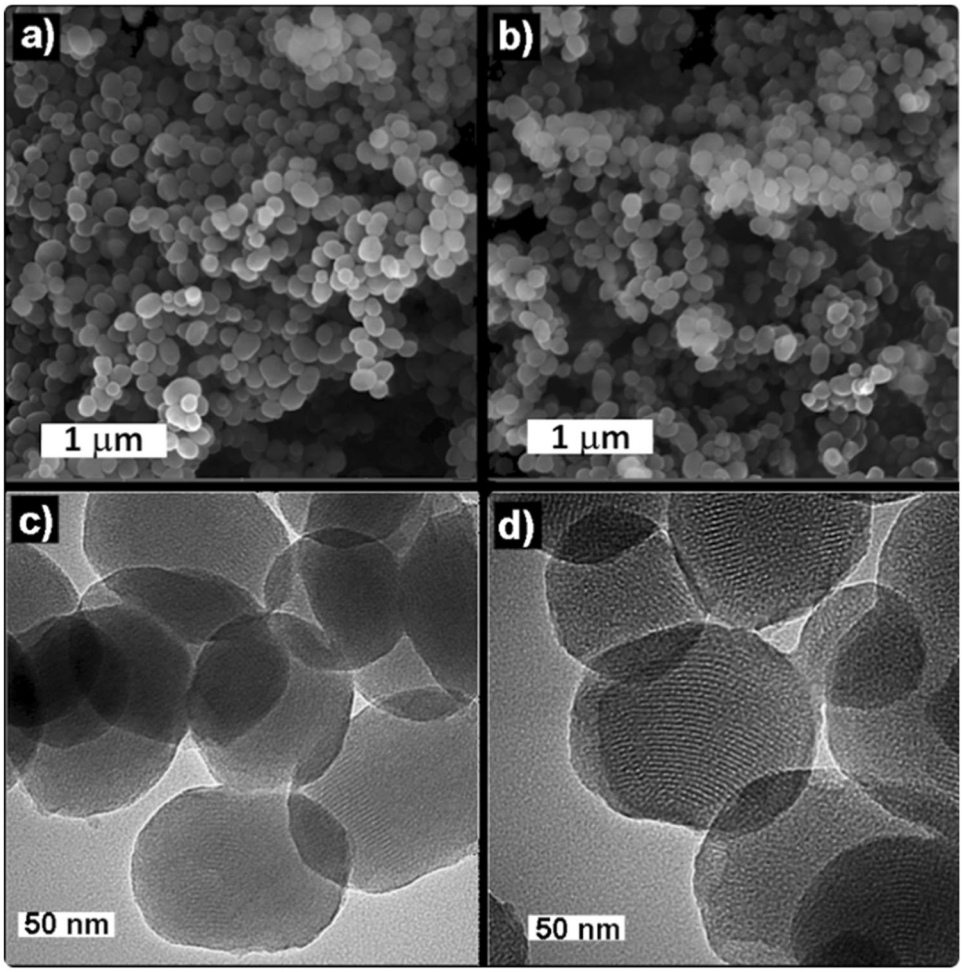

Fig. 1 SEM (**a**, **b**) and TEM (**c**, **d**) micrographs of MPMSN (**a**, **c**) and BMPH-MPMSN (**b**, **d**)

after functionalization (Table 1). However, the hydrodynamic diameter of GdB@BMPH-MPMSN is lower than for the materials before loading. It is possible that the presence of capping and loaded molecules help to disperse the particles better and hence the lower DLS size. Higher negative charge is also obtained for the GdB-loaded materials which surely helps to disperse the particles.

Nitrogen sorption measurements confirmed the functionalization of MPMSN with BMPH, as the surface area, calculated using the Brunauer, Emmett and Teller (BET) method, is reduced from 864 m^2/g to 773 m^2/g and the pore volume from 0.53 cm^3 to 0.47 cm^3 after functionalization. Both materials show the same predominant pore size peak at 1.9 nm and the average pore size at 2.4 nm (Table 2), determined following the Barrett, Joyner and Halenda (BJH) method. The isotherms of both materials are clearly type IV before loading (Fig. 3), without evident hystereses. However, after the loading of GdB and capping with CD-CHO and AA, the BET isotherm changes to type I, which is typical for microporous materials and demonstrates successful capping of the mesopores. The results of BJH also demonstrate this outcome (Fig. 3, inset). Notably, the mesopores that are evident in the noncapped material are clearly missing upon loading the GdB and capping the pores. BET specific surface area and pore volume also decrease to 224 ± 4 m^2/g and 0.20 ± 0.004, respectively. The amount of encapsulated GdB was 190.4 ± 2.9 mg/g material, as determined from the filtrates and the standard curves obtained through fluorescence spectroscopy (Supplementary Fig. S2), as detailed in the experimental section.

The release of GdB was monitored through fluorescence measurements in aqueous environment at different pH (Fig. 4a). The measurements were performed on supernatants, after removal of the materials by centrifugation at designated time points, with excitation at 280 nm and monitoring the emission at 312 nm. Evidently, the release of GdB is significantly enhanced in weakly acidic environment (pH 5.0) in comparison to the release at the higher pH values. It is noticeable, particularly at pH 5.0, that the amount of released GdB in supernatants decreases after the first measurement. It is possible that this effect is due to re-adsorption of GdB onto the surface of the materials after the initial release and possible interaction with the surface bound BMPH and thiol groups. A similar decreasing trend

after the initial burst release was noted in case of the pH-responsive release of anticancer drug Doxorubicin from the functionalized MSNs due to its reaction with the surface-bound groups [30]. The maximum release was noted after 30 min of stirring and determined to be 56.6 ± 7.4 milligrams of GdB per gram of the material (29.7 ± 3.9% of the loaded amount), as determined from the standard curve. In the case of 1 mg/mL suspension of GdB@BMPH-MPMSN, after 30 min, the concentration of released GdB was 91.0 ± 2.9 µM at pH 5.0.

We further evaluated the MRI capabilities of GdB@BMPH-MPMSN in weakly acidic vs. physiological pH condition. As shown in the pseudo-colored images of the supernatants after 48 h of incubation of the GdB loaded material at pH 5.0 and 7.4 (Fig. 4b), the measured relaxation at pH 5 is significantly enhanced in comparison to the relaxation of the supernatant at pH 7.4. The obtained values for longitudinal relaxation of the supernatants (Supplementary Fig. S4) for GdB@BMPH-MPMSN at pH 5 was 2.3 s, while the same material at 7.4 showed higher T_1 value of 2.6 s, in agreement with the lower release of GdB at the physiological pH condition. In comparison, the obtained supernatant T_1 values from the suspension of the material without loaded GdB (MPMSN) were notably higher (2.9 s).

Additional continuous MRI measurements were performed at different time points using the GdB@BMPH-MPMSN material suspended at high concentration (10 mg/mL) in buffers at pH 5.0 and 7.4 and compared to the suspension of MPMSN material as a negative control. In the applied highly concentrated suspension and without applying sonication, the nanoparticles tend to aggregate and sediment on the bottom of the measuring cuvettes. These conditions were used to evaluate possibilities for continuous measurement of the concentration of released GdB through analyzing the MRIs, without employing centrifugation for separating the nanoparticles. We measured longitudinal relaxation times (T_1) in the bottom area of the sedimented particles and at the top of the cuvettes-in the area of bulk solution, with the same region of interest (ROI) for all samples (Supplementary Fig. S5). The calculated values of T_1 in the area of the bulk solution above the sedimented GdB@BMPH-MPMSN revealed shorter T_1 in the case of the material at pH 5, vs the material at pH 7.4 at all measured time points ($p < 0.05$). These differences in T_1 in the bulk solution above the sedimented materials can be

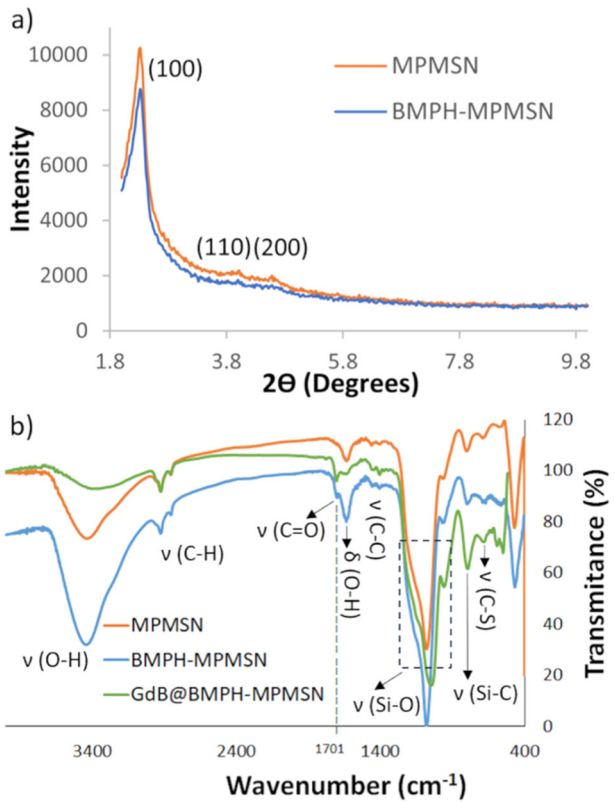

Fig. 2 **a** Low angle XRD and **b** FTIR of MPMSN, BMPH-MPMSN and GdB@BMPH-MPMSN

Table 1 Particle size and zeta potential of prepared materials

Material	Weight loss (% ± SD) between 300 and 700 °C	Hydrodynamic Diameter (nm ± SD)	Zeta potential (mV ± SD)
MPMSN	22.35 ± 0.13	250.9 ± 11.4	−23.5 ± 1.2
BMPH-MPMSN	23.38 ± 0.14	250.5 ± 7.4	−25.6 ± 0.6
GdB@BMPH-MPMSN	27.60 ± 0.17	206.0 ± 10.1	−41.7 ± 1.2

Table 2 BET and BJH characteristics of the starting materials

Material	Surface area (m^2/g ± SD)	BJH predominant peak (nm ± SD)	Average pore size (nm ± SD)	Total pore volume (cm^3/g ± SD)
MPMSN	864 ± 17	1.93 ± 0.04	2.44 ± 0.05	0.53 ± 0.01
BMPH-MPMSN	773 ± 15	1.90 ± 0.04	2.43 ± 0.05	0.47 ± 0.01

correlated with the enhanced release of GdB from the mesopores in weakly acidic conditions. Indeed, we determined the concentration of the released GdB in bulk solution from the obtained T_1 values based on the prepared standard curves of GdB at pH 5.0 and 7.4 (Fig. 4c, d). Evidently, higher GdB concentrations were noted in case of the samples at pH 5 with the highest concentration of GdB observed at the 1.5 h point at pH 5 (0.031 ± 0.03 mg/mL), while at pH 7.4, the same material released half of that GdB concentration (0.016 ± 0.006 mg/mL). All concentrations of the released GdB at pH 5.0 are significantly higher than the values at pH 7.4 ($p < 0.05$).

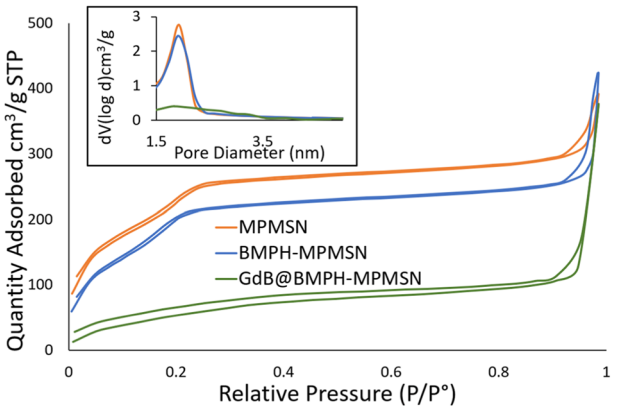

Fig. 3 **a** BET isotherms and BJH pore distribution (inset) of MPMSN, BMPH-MPMSN and GdB@BMPH-MPMSN

4 Discussion

Quantitative MRI measurements indicated that the release of GdB at pH 5.0 almost doubled compared to pH 7.4. Nevertheless, the released amounts of GdB in the MRI experiments are much lower than the values expected from the release kinetics measurements. This difference could be attributed to the fact that for the release kinetics studies, the suspensions of the materials at concentrations of 0.5 mg/mL were stirred vigorously, which produced the optimal conditions for the diffusion from the pores and maximum release of GdB (0.028 ± 0.009 mg/mL and 0.009 ± 0.005 mg/mL, at pH 5 and

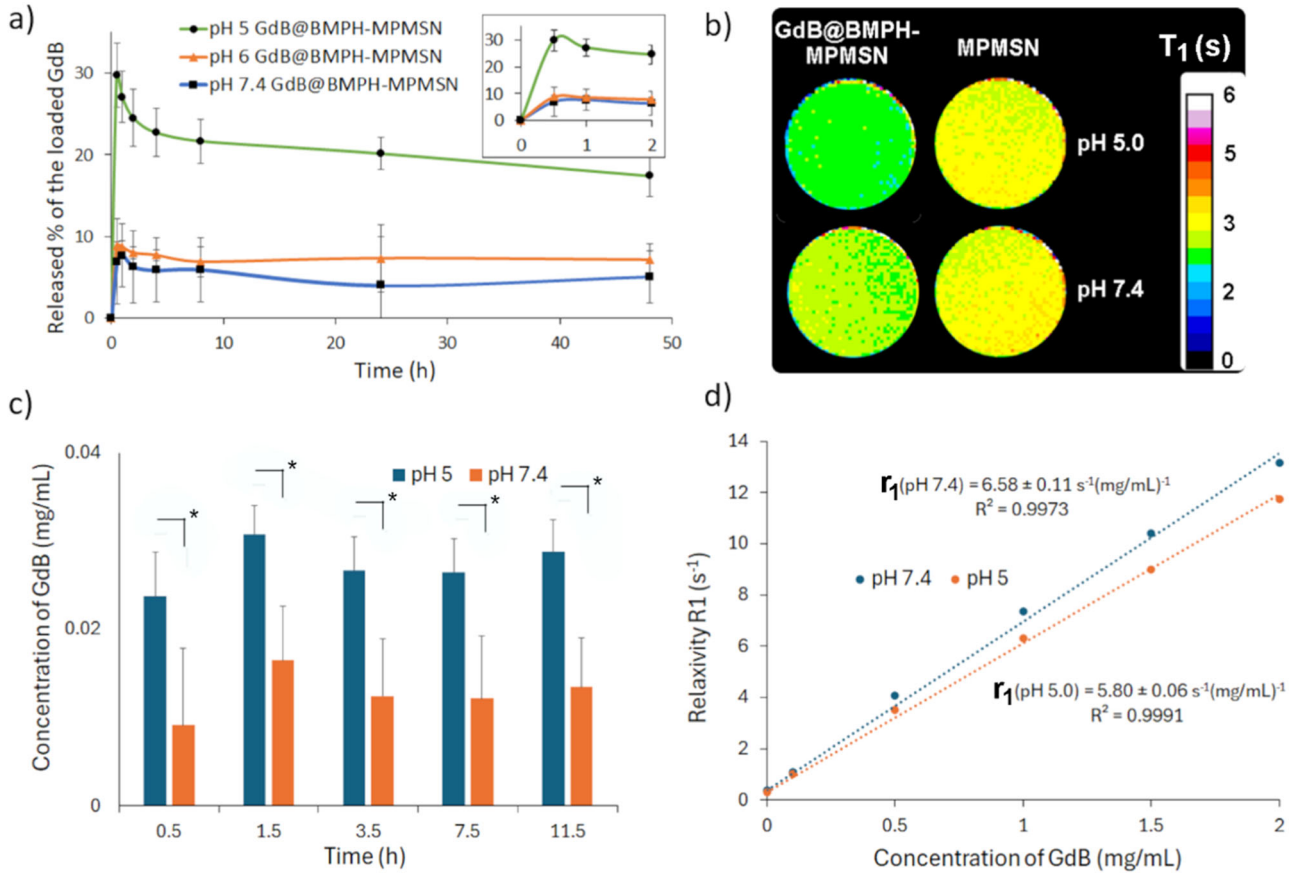

Fig. 4 **a** Release of GdB from GdB@BMPH-MPMSN at pH 5.0, 6.0, and 7.4. Inset shows the first two hours of GdB release. **b** T_1-maps (pseudo-colored) of supernatants after 48 of incubation of GdB@BMPH-MPMSN and MPMSN suspensions at pH 7.4 and pH 5; **c** Gadobutrol concentrations [mg/mL] ±SD in GdB@BMPH-MPMSN in the bulk solution (*$p < 0.05$) calculated based on (**d**) linear fitting of GdB known concentrations vs. longitudinal relaxation rate ($R_1 = 1/T_1$) for pH 5.0 and pH 7.4

pH 7.4 respectively). On the other hand, the MRI experiments were performed at a 20-fold higher concentration (10 mg/mL) without stirring, leading to low GdB diffusion efficiency from the mesopores and enhanced re-adsorption rate on the MSN surface.

Results of a recent study revealed that the signal intensity on T_1-weighted MR images of the material decreased upon the release of the CA from the mesopores [16]. This effect was ascribed to the low rotational tumbling time of the CAs within the mesopores [31]. As MSNs contained positively charged functional groups inside the mesopores and the CA (gadopentetate dimeglumine) was negatively charged the decrease in the tumbling rate of CAs occurred through electrostatic interactions inside the mesopores. However, the concept of monitoring the decrease of MRI signal intensity from this type of particles would be hardly suitable for in vivo applications, as the released CAs would typically bind to the biomolecules within the tissue, again decreasing their rotational tumbling time and enhancing the intensity of T_1-weighted MRI [32], which would negate the effect observed on the particles. On the contrary, the pores of BMPH-MPMSN in our study are loaded with non-charged GdB molecules and enhanced MR relaxation was not observed from the particles, accordingly. Hence, significantly lower signal MR intensity was observed for the CA-loaded MSNs in our study, even though the loading capacity of the CA in our study is only slightly lower (19%) in comparison to the published study on MSNs loaded with gadopentetate dimeglumine (24%). The low CA-capabilities of GdB loaded NPs were evident for the precipitated material on Supplementary Fig. S5, with the obtained same longitudinal relaxation times $T_1 = 1.7 \pm 0.1$ s, for the samples of GdB@BMPH-MPSN at both pH. Nevertheless, the low CA capabilities of GdB-loaded material might be beneficial for enabling detection of enhanced MR relaxation upon the release of GdB. In order to enhance the applicability of CA-loaded DDSs for MRI-based detection of cargo release, future optimization of the nanomaterial and the methodology is needed. The combination of the CA and the nanocarrier should be optimized to enhance the CA loading and release capacity, while maximizing the quenching and recovery of MR relaxation before and after the release, respectively.

Looking beyond the herein introduced proof of concept, the possible MRI monitoring of the release of CAs upon exposure to stimuli, such as acidification, might allow a real-time insight into the capabilities of the nanocarriers to deliver their therapeutic cargo to desired locations. Furthermore, the tracking of the changes in signal intensity upon the pH-responsive release of CAs could be applicable for MRI-based in vivo sensing of tissue pH and hence could be applicable in diagnosis of tissue acidosis and cancers, as well as for signaling the cellular uptake of nanoparticles in the late endosomes or lysosomes (pH ~ 4.5–5.5). Finally, other CA-loaded nanoparticles might be envisioned which could be applicable for monitoring different molecules capable of triggering the release of CAs [33].

5 Conclusions

The contrast agent GdB was successfully entrapped inside pH-responsive mesoporous silica-based nanomaterials. The released amounts of GdB were enhanced in weakly acidic conditions in comparison to the release at the physiological pH. The MRI measurements on buffered suspensions of the materials confirmed the capabilities of this methodology to identify enhanced release of CAs at weakly acidic conditions. The contribution of the obtained proof-of-concept results to the scientific literature is evident in terms of opening a promising novel methodology for using MRI for monitoring the release of cargo molecules from nanocarriers. This methodology could allow future applications in MRI-based sensing of pH, revealing endosomal internalization of nanoparticles, as well as for identifying drug delivery systems with optimized capabilities for cargo delivery to desired locations. Hence, contrast agent-loaded NPs could be applied in the future, prior to the treatment with the drug-filled analogs. This would allow rapid assessment of the ability of nanotherapeutics to release their therapeutic loading and reveal the biodistribution of the released cargo, which could effectively lead to a more personalized clinical management of cancer patients.

Supplementary information The online version contains supplementary material available at https://doi.org/10.1007/s10971-024-06422-9.

Acknowledgements The authors thank Dr. Aldrik Velders, Wageningen University and Research, for helpful discussions.

Author contributions Conceptualization, NŽK; methodology, NŽK, JL, MMun, OG, ERH; validation and formal analysis, MMun, JL, MMlad, AP, and AU; investigation, MMun, JL, MMlad; resources, MSM, ERH; writing—original draft preparation, MMun, and NŽK; writing—review and editing, MSM, ERH, JL, NŽK, OG; visualization, MMlad, AU, JL, AP; supervision, NŽK, MSM, OG; project administration, NŽK, MSM, ERH; funding acquisition, NŽK and ERH. All authors have read and agreed to the published version of the manuscript.

Funding The Science Fund of the Republic of Serbia, PROMIS, #6060755, PRECAST. The European Union's Horizon 2020 research and innovation program under grant agreement 952259 (NANOFACTS), the European Research Council under grant agreement 758887 (REACT) and the Ministry of Science, Technological development and Innovation of the Republic of Serbia (grant 451-03-66/2024-03/200358).

Compliance with ethical standards

Conflict of interest The authors declare no competing interests.

References

1. Mura S, Nicolas J, Couvreur P (2013) Stimuli-Responsive Nanocarriers for Drug Delivery. Nat Mater 12:991–1003. https://doi.org/10.1038/nmat3776
2. de la Torre C, Coll C, Ultimo A, Sancenón F, Martínez-Máñez R, Ruiz-Hernández E (2023) In Situ-Forming Gels Loaded with Stimuli-Responsive Gated Mesoporous Silica Nanoparticles for Local Sustained Drug Delivery. Pharmaceutics 15:1071. https://doi.org/10.3390/pharmaceutics15041071
3. Živojević K, Mladenović M, Djisalov M, Mundzic M, Ruiz-Hernandez E, Gadjanski I, Knežević NŽ (2021) Advanced Mesoporous Silica Nanocarriers in Cancer Theranostics and Gene Editing Applications. J Control Rel 337:193–211. https://doi.org/10.1016/j.jconrel.2021.07.029
4. van Elk M, Murphy BP, Eufrásio-da-Silva T, O'Reilly DP, Vermonden T, Hennink WE, Duffy GP, Ruiz-Hernández E (2016) Nanomedicines for Advanced Cancer Treatments: Transitioning towards Responsive Systems. Int J Pharm 515:132–164. https://doi.org/10.1016/j.ijpharm.2016.10.013
5. Zhang E, Bandera Y, Dickey A, Foulger I, Kolis JW, Foulger SH (2021) Development of dispersible radioluminescent silicate nanoparticles through a sacrificial layer approach. J Colloid Interf Sci 582:1128–1135. https://doi.org/10.1016/J.JCIS.2020.07.125
6. Marcelo GA, Galhano J, Oliveira E (2023) Applications of cyanine-nanoparticle systems in science: Health and environmental perspectives. Dyes Pigments 208:110756. https://doi.org/10.1016/J.DYEPIG.2022.110756
7. Yan D, Qin Y, Yan S, Sun P, Wang Y, Wang D, Tang BZ (2023) Near-infrared emissive AIE nanoparticles for biomedical applications: From the perspective of different nanocarriers. Particuology 74:103–118. https://doi.org/10.1016/J.PARTIC.2022.06.001
8. Llop J, Lammers T (2021) Nanoparticles for Cancer Diagnosis, Radionuclide Therapy and Theranostics. ACS Nano 15:16974–16981. https://doi.org/10.1021/acsnano.1c09139
9. Smith L, Byrne HL, Waddington D, Kuncic Z (2022) Nanoparticles for MRI-guided radiation therapy: a review. Cancer Nanotechnol 13:38. https://doi.org/10.1186/s12645-022-00145-8
10. Li Z, Guo J, Qi G, Zhang M, Hao L (2022) pH-Responsive Drug Delivery and Imaging Study of Hybrid Mesoporous Silica Nanoparticles. Molecules 27:6519. https://doi.org/10.3390/molecules27196519
11. Kato Y, Ozawa S, Miyamoto C, Maehata Y, Suzuki A, Maeda T, Baba Y (2013) Acidic extracellular microenvironment and cancer. Cancer Cell Int 13:89. https://doi.org/10.1186/1475-2867-13-89
12. Halcrow P;, Datta G;, Ohm JE;, Soliman ML;, Chen X;, Geiger JD (2019) Role of endolysosomes and pH in the pathogenesis and treatment of glioblastoma. Cancer Rep. 2:e1177. https://doi.org/10.1002/cnr2.1177
13. Such GK, Yan Y, Johnston AP, Gunawan ST, Caruso F (2015) Interfacing materials science and biology for drug carrier design. Adv Mater 27:2278–2297. https://doi.org/10.1002/adma.201405084
14. Seo H, Ma KY, Tuttle EE, Calderon IAC, Buskermolen AD, Flask CA, Clark HA (2021) A DNA-Based MRI Contrast Agent for Quantitative pH Measurement. ACS Sens 6(3):727–732. https://doi.org/10.1021/acssensors.1c00296
15. Lu H, Chen A, Zhang X, Wei Z, Cao R, Zhu Y, Lu J, Wang Z, Tian L (2022) A pH-responsive T1-T2 dual-modal MRI contrast agent for cancer imaging. Nat Commun 13:7948. https://doi.org/10.1038/s41467-022-35655-x
16. Cheng C-A, Chen W, Zhang L, Wu HH, Zink JI (2019) A Responsive Mesoporous Silica Nanoparticle Platform for Magnetic Resonance Imaging-Guided High-Intensity Focused Ultrasound-Stimulated Cargo Delivery with Controllable Location, Time, and Dose. J Am Chem Soc 141:17670–17684. https://doi.org/10.1021/jacs.9b07591
17. Knežević NŽ, Kaluderović GN (2017) Silicon-Based Nanotheranostics. Nanoscale 9:12821–12829. https://doi.org/10.1039/c7nr04445c
18. Rahikkala A, Pereira SAP, Figueiredo P, Passos MLC, Araújo ARTS, Saraiva MLMFS, Santos HA (2018) Mesoporous Silica Nanoparticles for Targeted and Stimuli-Responsive Delivery of Chemotherapeutics: A Review. Adv Biosyst 2:1800020. https://doi.org/10.1002/adbi.201800020
19. Knežević NŽ, Durand J-O (2015) Targeted Treatment of Cancer with Nanotherapeutics Based on Mesoporous Silica Nanoparticles. Chempluschem 80:26–36. https://doi.org/10.1002/cplu.201402369
20. Lu J, Liong M, Li Z, Zink JI, Tamanoi F (2010) Biocompatibility, Biodistribution, and Drug-Delivery Efficiency of Mesoporous Silica Nanoparticles for Cancer Therapy in Animals. Small 6:1794–1805. https://doi.org/10.1002/smll.201000538
21. Lérida-Viso A, Estepa-Fernández A, García-Fernández A, Martí-Centelles V, Martínez-Máñez R (2023) Biosafety of mesoporous silica nanoparticles; towards clinical translation. Adv Drug Deliv Rev 201:115049. https://doi.org/10.1016/J.ADDR.2023.115049
22. Wu Y, Xu Z, Sun W, Yang Y, Jin H, Qiu L, Chen J, Chen J (2019) Co-responsive smart cyclodextrin-gated mesoporous silica nanoparticles with ligand-receptor engagement for anti-cancer treatment. Mater Sci Eng C 103:109831. https://doi.org/10.1016/J.MSEC.2019.109831
23. Zhao Y-L, Li Z, Kabehie S, Botros YY, Stoddart JF, Zink JI (2010) pH-Operated Nanopistons on the Surfaces of Mesoporous Silica Nanoparticles. J Am Chem Soc 132:13016–13025. https://doi.org/10.1021/ja105371u
24. Kalia J;, Raines RT (2008) Hydrolytic stability of hydrazones and oximes. Angew Chem Int Ed 47:7523–7526. https://doi.org/10.1002/anie.200802651
25. Noureddine A, Lichon L, Maynadier M, Garcia M, Gary-Bobo M, Zink JI, Cattoën X, Wong Chi Man M (2015) Controlled multiple functionalization of mesoporous silica nanoparticles: homogeneous implementation of pairs of functionalities communicating through energy or proton transfers. Nanoscale 7(26):11444–11452. https://doi.org/10.1039/c5nr02620b
26. Lis-Cieplak A, Sitkowski J, Kolodziejski W (2013) Comparative Proton Nuclear Magnetic Resonance Studies of Amantadine Complexes Formed in Aqueous Solutions with Three Major Cyclodextrins. J Pharm Sci 103:274–282. https://doi.org/10.1002/jps.23802
27. Cornwell MJ, Huff JB, Bieniarz C (1995) A One-Step Synthesis of Cyclodextrin Monoaldehydes. Tetrahedron Lett 36:8371–8374. https://doi.org/10.1016/0040-4039(95)01808-U

28. Jiang L, Wang Z, Wang Y, Liu S, Xu Y, Zhang C, Li L, Si S, Yao B, Dai W, Li H (2023) Re-exposure of chitosan by an inhalable microsphere providing the re-education of TAMs for lung cancer treatment with assistant from sustained H2S generation. Int J Pharm 642:123142. https://doi.org/10.1016/J.IJPHARM.2023.123142
29. Knežević NŽ, Trewyn BG, Lin VS-Y (2011) Functionalized Mesoporous Silica Nanoparticle-Based Visible Light Responsive Controlled Release Delivery System. Chem Commun 47:2817–2819. https://doi.org/10.1039/c0cc04424e
30. Knežević NŽ, Trewyn BG, Lin VS-Y (2011) Light- and pH-Responsive Release of Doxorubicin from a Mesoporous Silica-Based Nanocarrier. Chem Eur J 17:3338–3342. https://doi.org/10.1002/chem.201002960
31. Manus LM, Mastarone DJ, Waters EA, Zhang X-Q, Schultz-Sikma EA, MacRenaris KW, Ho D, Meade TJ (2010) Gd(III)-Nanodiamond Conjugates for MRI Contrast Enhancement. Nano Lett 10:484–489. https://doi.org/10.1021/nl903264h
32. Wang Y, Spiller M, Caravan P (2010) Evidence for weak protein binding of commercial extracellular gadolinium contrast agents. Magn Reson Med 63:609–616. https://doi.org/10.1002/mrm.22214
33. Vallet-Regí M, Schüth F, Lozano D, Colilla M, Manzano M (2022) Engineering Mesoporous Silica Nanoparticles for Drug Delivery: Where Are We after Two Decades? Chem Soc Rev 51:5365–5451. https://doi.org/10.1039/D1CS00659B